Solar Energy 225 (2021) 842–850

Contents lists available at ScienceDirect

Solar Energy

journal homepage: www.elsevier.com/locate/solener

Numerical simulation analysis towards the effect of charge transport layers electrical properties on cesium based ternary cation perovskite solar cells performance

Ehsan Raza [a], Zubair Ahmad [b,*], Fakhra Aziz [c], Muhammad Asif [a], Ayyaz Ahmed [d], Kashif Riaz [d], Jolly Bhadra [b], Noora J. Al-Thani [b]

[a] Department of Electronics, University of Peshawar, Peshawar 25120, Pakistan
[b] Qatar University Young Scientists Center (QUYSC), Qatar University, 2713 Doha, Qatar
[c] Department of Electronics, Jinnah College for Women, University of Peshawar, Peshawar 25120, Pakistan
[d] Department of Electrical Engineering, Information Technology University (ITU), 346-B, Ferozepur Road, Lahore, Pakistan

ARTICLE INFO

Keywords:
Device simulation
Inverted perovskite solar cells
Doping concentration
Defect density
Charge transport layers
Triple (Cs/FA/MA) cation

ABSTRACT

In the present study, the device modeling of inverted architecture based on ITO/HTL/perovskite absorber/ETL/Ag was performed using a one-dimensional solar cell capacitance simulation (SCAPS-1D) program. Initially, device performance was evaluated with the experimental reported structure ($NiOx/Cs_x(MA_{0.17}FA_{0.83})_{1-x}Pb(I_{0.83}Br_{0.17})_3$/PCBM) to extract optimum parameters of each layer. Then, further optimization was carried out using a comparative study of six hole transport layers (HTLs) and six electron transport layers (ETLs). Among the investigated ETLs and HTLs, CuI (HTL) and CdZnS (ETL) were chosen due to their better performance. In addition, the parameters of the perovskite layer, such as thickness variation, defect density, and defect energy level, have been optimized to analyze the device performance. Similarly, doping concentrations of the perovskite, CuI, and CdZnS were varied, and their influence on device performance was examined. Results revealed that for an efficient inverted PSC design, a thickness of 600 nm of the perovskite is suitable. Moreover, the best-optimized values for defect density and defect energy level were found as 2.6×10^{13} cm^{-3} and 0.1 eV, respectively. Similarly, doping concentrations of 10^{17} cm^{-3} for the absorber, 10^{20} cm^{-3} for the CuI and CdZnS are the best-optimized values. With these optimized values, our results demonstrated a PCE of 22.99%.

1. Introduction

Perovskite solar cells (PSCs) composed of organic-inorganic metal halide structures have obtained substantial research interest from the scientific community towards cost-effective and high-performance photovoltaic (PV) applications. These materials possess several key features such as light absorption through a broad-spectrum range (Li et al., 2018), direct and tunable bandgap (Ou et al., 2019), long charge carriers diffusion lengths (Giovanni et al., 2021), and excellent carrier mobilities (Bahtiar et al., 2018). With these outstanding characteristics, the efficiency values increased dramatically from 3.8% in 2009 (Kojima et al., 2009) to over 25% in 2021 (Jeong et al., 2021). A large amount of work has been accomplished among the reported work on methyl-ammonium lead tri-iodide ($MAPbI_3$) perovskite composition (Khattak et al., 2020). However, the degradation under moisture and instability issues at ~55 °C associated with this class of material limits their

Abbreviations: E_A, Activation energy; CBO, Conduction band offset; CdZnS, Zinc Cadmium Sulfide; CuI, Copper Iodide; Cu_2O, Copper (I) Oxide; CuSCN, Copper thiocyanate; Cs, Cesium; ELIS, Electronics and Information Systems; ETL, Electron transport layer; EQE, External quantum efficiency; eV, Electron volt; FA, Formamidimium; FF, Fill factor; G, Generation rate; h, Hole concentration; HTL, Hole transport layer; ITO, Indium tin oxide; J_n, Current density for Electron; J_p, Current density for Hole; Jsc, Short circuit current density; MA, Methylammonium; N_A, Doping concentration for acceptor; N_D, Doping concentration for donor; NiO, Nickel Oxide; NREL, National Renewable Energy Laboratory; Nt, Number of defects; p, Electron concentration; PbI, Lead Iodide; PCE, Power conversion efficiency; PSC, Perovskite Solar Cell; PTAA, Poly[bis(4-phenyl)(2,4,6-trimethylphenyl)amine; PV, Photovoltaic; p_h, Hole distribution; p_e, Electron distribution; q, Electric Charge; R, Recombination rate; Rs, Series resistance; Rsh, Shunt resistance; SCAPS-1D, One Dimensional Solar Cell Capacitance Simulator; VBO, Valence band offset; UV, Ultravoilet; V_{bi}, Built-in voltage; Voc, Open circuit voltage; ZnO, Zinc Oxide.

* Corresponding author.
E-mail address: zubairtarar@qu.edu.qa (Z. Ahmad).

https://doi.org/10.1016/j.solener.2021.08.008
Received 27 June 2021; Received in revised form 29 July 2021; Accepted 2 August 2021
Available online 7 August 2021

potential employment in a broad range of applications (Akbulatov et al., 2021). The replacement of formamidinium (FA) with methylammonium (MA) has improved the moisture instability problem. However, $FAPbI_3$ undergoes two different phases at room temperature, making this class of material unsuitable in the long run (Chen et al., 2021; Ye et al., 2017). With the emergence of inorganic cesium (Cs) into mixed cations and halides compositions with FA and MA, the instability issues have been addressed considerably (Ašmontas et al., 2021; Bai et al., 2019). This new class of material has gained significant consideration from scientific society to unlock its additional properties further and improve PSCs performance.

The structure of PSC consists of front contact, an electron-transport layer (ETL), an active layer, a hole-transport layer (HTL), and a back metal contact. When light is incident on the PSC, the charge carriers are created in the active layer. ETLs and HTLs transport these photo-generated charge carriers to their respective electrodes. In contrast to the role of the perovskite layer, the significance of charge transport layers (crucial components of PSCs) is of vital importance towards the overall device performance of PSCs. For instance, spiro-OMeTAD is extensively employed as an HTL in PSCs. However, such HTL suffers from low conductivity and hole mobility in pristine form, which can be improved by introducing various dopants (Wang et al., 2020).

On the other hand, the addition of dopants raises the overall cost of such HTLs. It degrades PSCs, restricting the employment of spiro-OMeTAD towards PSCs commercialization (W.W. Liu et al., 2019). Similarly, a widely used ETL, namely TiO_2, requires an operating temperature of over 450 °C, which is inappropriate for large area device fabrication (Ahmed et al., 2020). In addition, low electron mobility and ultraviolet (UV) instability of TiO_2 restrict their application in high-performance PSCs (Raoui et al., 2019). Therefore, it is highly desirable to search for potential charge transport layers having promising capabilities, such as high charge carrier mobilities, high conductivity, and low-temperature processing.

Planar PSCs are of two types, regular “n-i-p” and inverted “p-i-n”. Reports found that the inverted structures demonstrate less hysteresis than regular designs (Jeon et al., 2014; X. Liu et al., 2019; Meng et al., 2016). Moreover, the inverted structures offer superiority compared to their counterparts in cost-effectiveness, low-temperature processing using a slot die coating, roll-to-roll printing, and compatibility with large area device fabrications (Liu et al., 2016). However, as per recently published records, PCE values in inverted single-junction structures lag behind regular PSCs, i.e., 22.8% and 25.6% (25.2% certified value), respectively (Alsalloum et al., 2021; Jeong et al., 2021). In addition, the highly efficient (22.8% PCE) inverted PSC employed C_{60}/BCP as ETL and PTAA as HTL. However, the high cost and degradation under UV irradiation associated with PTAA are still debatable (Petrović et al., 2019). Therefore, to improve the overall performance of inverted PSCs using potential ETLs and HTLs, to understand the physical parameters, and to overcome recombination losses mechanisms, a numerical study is essential.

In this study, we reproduced the results of experimentally reported 15.51% efficient and stable single cation-based structure (ITO/NiO/$MAPbI_3$/PCBM/Ag) and 12.6% efficient hysteresis less triple cation-based structure (ITO/NiO_x/$Cs_x(MA_{0.17}FA_{0.83})_{1-x}Pb(I_{0.83}Br_{0.17})_3$/$PC_{60}BM$/Ag) to validate our measurements (Qiu et al., 2017; Weber et al., 2018). A considerable amount of work has been performed on single cation PSCs through simulation, while negligible work has been done so far on triple cation PSCs. Therefore, we considered a triple cation-based structure as a reference cell and enhanced the overall device performance. Initially, a comparative study of six ETLs and six HTLs was performed. Different ETLs studied here include cadmium sulfide (CdS), fullerene (C_{60}), cadmium zinc sulfide (CdZnS), titanium dioxide (TiO_2), phenyl-C61-butyric acid methyl ester (PCBM), and zinc oxide (ZnO). Similarly, cuprous oxide (Cu_2O), poly[bis(4-phenyl)(2,4,6-trimethylphenyl)amine (PTAA), nickel oxide (NiO_x), copper thiocyanate (CuSCN), poly(3,4-ethylenedioxythiophene) polystyrene sulfonate (PEDOT:PSS) and copper(I) iodide (CuI) were investigated as HTLs. The thickness variation of the absorber was further analyzed to enhance the reference PSC performance. Besides thickness variation, defect density, defect density energy level, doping concentration of absorber, and best-optimized HTL and ETL were also optimized, and their influence on PSC performance was explored.

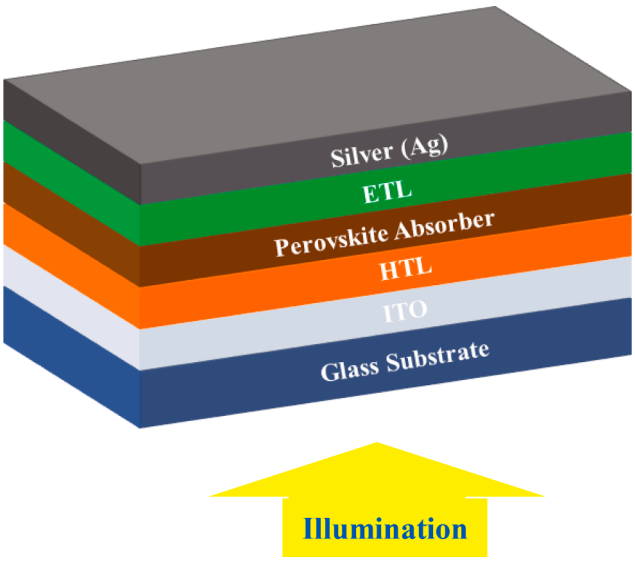

Fig. 1. Schematic of the simulated cesium based inverted triple cation (Cs/FA/MA) PSC.

2. Device simulation parameters and methodology

The one-dimensional device simulator solar cell capacitance simulator structure (SCAPS-1D, ver. 3.3.07) was employed in this work. It was designed by the Electronics and Information Systems (ELIS) Department at the University of Gent, Belgium (Burgelman et al., 2000).

Table 1
Device parameters of simulated perovskite solar cell.

Parameters	HTL (NiO_x)	Perovskite Absorber ($Cs_x(MA_{0.17}FA_{0.83})_{1-x}Pb(I_{0.83}Br_{0.17})_3$)	ETL ($PC_{60}BM$)
Thickness (nm)	34 (Variable)	320 (Variable)	50 (Variable)
Bandgap E_g (eV)	3.64 (Weber et al., 2018)	1.62 (Weber et al., 2018)	1.8 (Weber et al., 2018)
Electron affinity χ (eV)	1.85 (Weber et al., 2018)	3.88 (Weber et al., 2018)	4.2 (Weber et al., 2018)
Dielectric permittivity ε_r	11.75 (Zhao et al., 2018)	6.5 (Minemoto et al., 2019)	4 (Zhao et al., 2018)
CB effective density of states N_c (cm^{-3})	2.50×10^{20} (Zhao et al., 2018)	2.50×10^{20} (Zhao et al., 2018)	1.0×10^{21} (Zhao et al., 2018)
VB effective density of states N_v (cm^{-3})	2.50×10^{20} (Zhao et al., 2018)	2.50×10^{20} (Zhao et al., 2018)	2×10^{20} (Zhao et al., 2018)
Electron thermal velocity (cm/s)	1.0×10^7	1.0×10^7	1.0×10^7
Hole thermal velocity (cm/s)	1.0×10^7	1.0×10^7	1.0×10^7
Electron mobility μ_n (cm^2/vs)	0.001 (Zhao et al., 2018)	2.0 (Minemoto et al., 2019)	0.01 (Zhao et al., 2018)
Hole mobility μ_p (cm^2/vs)	0.001 (Zhao et al., 2018)	2.0 (Minemoto et al., 2019)	0.01 (Zhao et al., 2018)
Shallow uniform acceptor density N_A (cm^{-3})	0	1.0×10^{13} (Variable)	1×10^{17} (Variable)
Shallow uniform donor density N_D (cm^{-3})	1×10^{18} (Variable)	0	0

Table 2
Defect parameters of different layers of simulated PSC (Minemoto et al., 2019).

Parameters	*HTL (NiO_x)*	*Perovskite Absorber ($Cs_x(MA_{0.17}FA_{0.83})_{1-x}Pb(I_{0.83}Br_{0.17})_3$)*	*ETL ($PC_{60}BM$)*
Type of Defect	Neutral	Neutral	Neutral
Electrons Capture Cross Section (cm^2)	2×10^{-14}	2×10^{-14}	2×10^{-14}
Holes Capture Cross Section (cm^2)	2×10^{-14}	2×10^{-14}	2×10^{-14}
Energetic Distribution	Gaussian	Gaussian	Gaussian
Defect Energy level Reference E_t	Above E_V	Above E_V	Above E_V
Energy level related to Reference (eV)	0.6	0.6 (Variable)	0.6
N_t (cm^{-3})	1×10^{15}	2.60×10^{13} (Variable)	1×10^{15}

Table 3
Parameters for interface layers of simulated reference perovskite solar cell (Shamna et al., 2020).

Interface layer	**HTL/perovskite absorber**	**Perovskite absorber/ETL**
Type of Defect	Neutral	Neutral
Electrons Capture cross section (cm^2)	1×10^{-19}	1×10^{-19}
Holes Capture cross section (cm^2)	1×10^{-19}	1×10^{-19}
Energetic distribution	Single	Single
Defect energy level Reference Et	Above the highest E_V	Above the highest E_V
Energy level related to reference (eV)	0.600	0.600
Total density -integrated over all energies- (cm^{-2})	1×10^{10}	1×10^{10}

It is designed based on three different equations, which include Poisson's equation (1), continuity equations for electrons (2), and holes (3).

$$\frac{d^2}{dx^2}\psi(x) = \frac{q}{\varepsilon}[p(x) - n(x) + N_D - N_A + p_h - p_e] \quad (1)$$

$$\frac{dJ_n}{dx} = G - R \quad (2)$$

$$\frac{dJ_p}{dx} = G - R \quad (3)$$

Here, ψ, q, ε, p, n, N_D, N_A, p_h, p_e, J_n, J_p, G, and R denote electrostatic potential, electric charge, dielectric constant, hole concentration, electron concentration, doping concentration for the donor, doping concentration for acceptor, hole distribution, electron distribution, current density for electron, current density for the hole, generation and recombination rates for carriers, respectively.

Fig. 1 displays the device schematic of our reference cell investigated in this work. Here, HTL represents NiO_x, ETL represents $PC_{60}BM$, perovskite absorber is based on $Cs_x(MA_{0.17}FA_{0.83})_{1-x}Pb(I_{0.83}Br_{0.17})_3$, whereas ITO and Ag served as front contact and back metal contact, respectively. The basic device parameters and absorption files of various materials used in this simulation were obtained from the literature (Ahmed et al., 2020; Chowdhury et al., 2020; Coulibaly et al., 2019; Dixit et al., 2019; Firdaus et al., 2018; Hima and Lakhdar, 2020; Hoppe et al., 2003; Lakhdar and Hima, 2020; Lin et al., 2019; Malerba et al., 2011; Minemoto et al., 2019; Raoult et al., 2019; Shamna et al., 2020; Zhao et al., 2018) and are summarized in Tables 1-3 and Table S2 and Table S5. The thickness of each layer was obtained from the literature reporting 12.6% efficiency with inverted configuration (Weber et al., 2018). The HTL/perovskite and perovskite/ETL interface defects were introduced in the simulation study. The simulation study was performed under the temperature of 300 K and the standard AM 1.5 G spectrum.

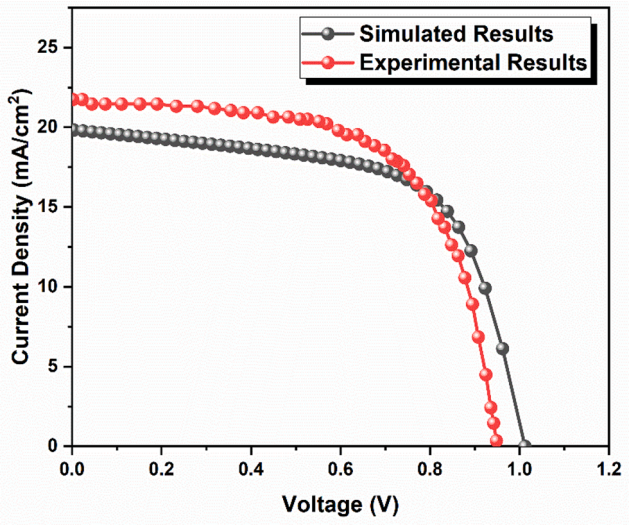

Fig. 2. A graphical comparison between experimental and reproduced simulated results of our reference PSC.

3. Results and discussion

3.1. Experimental and simulated results comparison

Fig. 2 depicts simulated and experimental results comparison of the reference cell. For the single cation perovskite composition, the comparison results are drawn in Fig. S1. According to Fig. S1 and Fig. 2, our simulated values are in decent agreement and close to the experimental values. A detailed comparison between simulated and experimental results in terms of J-V parameters (J_{SC}, V_{OC}, FF & PCE) for single cation and triple cation compositions are provided in Table S1 and Table 4, respectively. A minor difference between the simulated and experimental values is that the ITO and Ag layers were used as front and back contacts in the current study, where we can't change the thickness of front and back contacts. In contrast, they were used as layers with proper thicknesses in the experimental work.

3.2. Influence of different ETLs on the PSC performance using NiO_x as HTL

The ETL has a significant influence on PSC performance. It transports negative charge carriers (photo-generated) from the absorber to the respective electrode while preventing the flow of holes. Then these electrons move into the external circuit to contribute to the formation of electric current. To obtain better performance of our reference cell, different ETLs are proposed. The reference PSC was employed with different ETLs (PCBM, CdZnS, CdS, ZnO, TiO_2, and C_{60}) of constant thicknesses while keeping NiO_x as HTL. The parameters are summarized in Table S2. The effect of these ETLs on PSC performance has been investigated. The plotted J-V characteristics are shown in Fig. 3(a), and the external quantum efficiency (EQE) data are plotted in Fig. 3(b), while Table 5 summarizes the J-V parameters. The corresponding energy band diagram of NiO_x, absorber and different ETLs is demonstrated in Fig. S2. It can be concluded from Table 5 that the CdZnS achieved the best device performance, followed by ZnO and TiO_2. However, the CdZnS delivers comparatively higher Jsc due to its higher carrier mobilities, achieving a higher PCE value. From the EQE data, it is observed that there is no difference in optical absorption of ETLs in the visible range as the ETLs are positioned at the backside of the PSC. The energy band diagram in Fig. S2 indicates that these three layers have appropriate band alignment with the absorber layer, which improved the overall device performance. Our results could be better explained by considering the conduction band offset (CBO) relative to the perovskite/

Table 4
A detailed comparison between device parameters of experimental and simulated results of Cs based triple cation reference perovskite solar cell.

	Eg (eV)	J_{SC} (mA/cm^2)	V_{OC} (V)	FF (%)	PCE (%)	R_S (Ω-cm^2)	R_{SH} (Ω-cm^2)
Experimental	1.62	21.7	0.94	62.8	12.80	4.9	355
Simulated		19.76	1.01	63.0	12.60	4.9	355

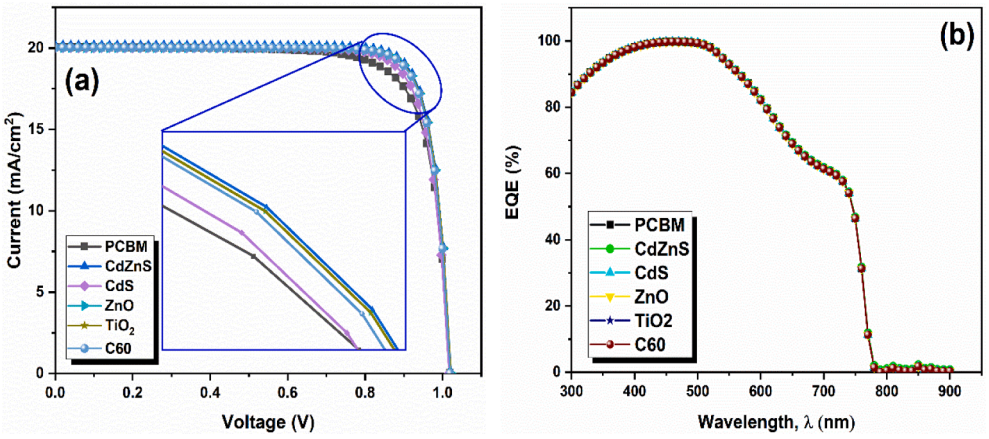

Fig. 3. (a) J-V characteristics of inverted PSC with NiO_x as HTL while PCBM, CdZnS, CdS, ZnO, TiO_2 and C_{60} as ETLs (b) simulated EQE curves of PCBM, CdZnS, CdS, ZnO, TiO_2 and C_{60} as ETLs.

Table 5
Performance of different ETLs with NiO_x as HTL and $Cs_x(MA_{0.17}FA_{0.83})_{1-x}Pb(I_{0.83}Br_{0.17})_3$ as perovsktie absorber.

Device configuration	J_{SC} (mA/cm^2)	V_{OC} (V)	FF (%)	PCE (%)
ITO/NiO_x/Perovskite Absorber/PCBM/Ag	20.03	1.01	78.21	15.97
ITO/NiO_x/Perovskite Absorber/CdZnS/Ag	20.16	1.02	83.52	17.21
ITO/NiO_x/Perovskite Absorber/CdS/Ag	20.02	1.01	81.58	16.61
ITO/NiO_x/Perovskite Absorber/ZnO/Ag	20.02	1.02	83.52	17.08
ITO/NiO_x/Perovskite Absorber/TiO_2/Ag	20.02	1.02	83.52	17.08
ITO/NiO_x/Perovskite Absorber/C_{60}/Ag	20.02	1.01	83.48	17.05

ETL interface with bandgap alignment and activation energy of (E_A) ETLs. The difference in electron affinity of ETL (χ_{ETL}) and perovskite absorber ($\chi_{Perovskite}$) is known as the CBO, whereas the activation energy is defined as E_A = Eg - |CBO| (Ahmed et al., 2020). The CBO and E_A values are tabulated in Table S3 and Table S4, respectively. The results of these two tables indicate that CdZnS has a CBO of +0.17, which is the highest among all investigated ETLs. This high value of CBO, along with higher carrier mobilities, results in increased Jsc and Voc. In addition, the E_A value significantly influences the performance of PSC. Low values of the CBO cause low E_A, which increases interface recombination, limiting the flow of electrons at the perovskite/ETL interface and hence reduced Voc. Whereas the positive value of CBO increases, the E_A causes reduced interface recombination, enhances the Voc, and thus high PCE. Table S4 indicates that both CdZnS and ZnO have higher E_A values relative to other ETLs. Whereas, E_A value for ZnO is 0.17 eV higher than CdZnS. However, due to positive CBO and higher carrier mobilities, the performance of CdZnS is comparatively best among all ETLs.

Previous reports revealed the best results with an optimized thickness of 40–50 nm for CdZnS (Ahmed et al., 2020; Chowdhury et al.,

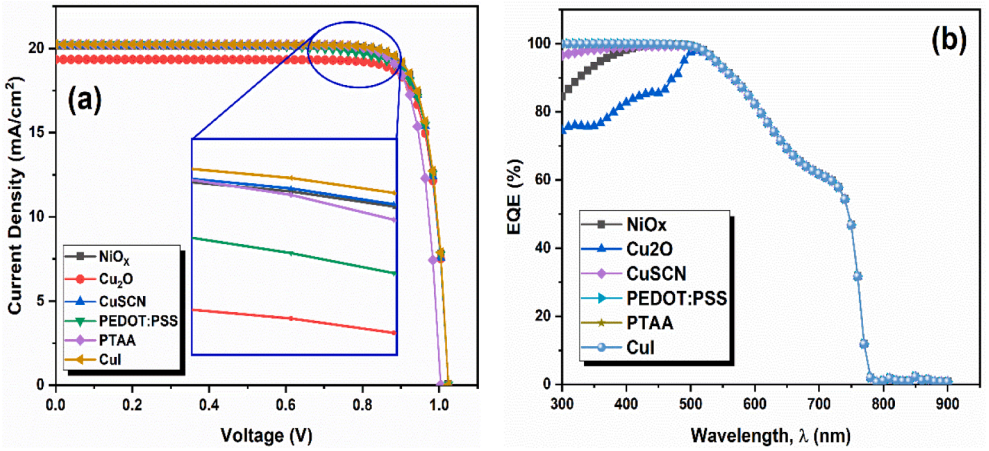

Fig. 4. (a) J-V characteristics of inverted PSC with CdZnS as ETL while NiOx, Cu2O, CuSCN, PEDOT:PSS, PTAA and CuI as HTLs (b) simulated EQE curves of NiOx, Cu2O, CuSCN, PEDOT:PSS, PTAA and CuI as HTLs.

Table 6
Performance of different HTLs with CdZnS as ETL and $Cs_x(MA_{0.17}FA_{0.83})_{1-x}Pb(I_{0.83}Br_{0.17})_3$ as perovsktie absorber.

Device configuration	J_{SC} (mA/cm^2)	V_{OC} (V)	FF (%)	PCE (%)
ITO/NiO_x/Perovskite Absorber/PCBM/Ag	20.16	1.02	83.52	17.21
ITO/Cu_2O/Perovskite Absorber/PCBM/Ag	19.35	1.02	83.57	16.52
ITO/CuSCN/Perovskite Absorber/PCBM/Ag	20.19	1.01	83.35	17.05
ITO/PEDOT:PSS/Perovskite Absorber/PCBM/Ag	20.26	1.02	81.35	16.88
ITO/PTAA/Perovskite Absorber/PCBM/Ag	20.24	1.01	83.16	17.03
ITO/CuI/Perovskite Absorber/PCBM/Ag	20.24	1.02	83.60	17.33

2018). Therefore, we considered 50 nm thick CdZnS as ETL and performed further device optimization in the current work.

3.3. *Influence of different HTLs on the PSC performance using CdZnS as ETL*

The influence of HTL on device performance is of vital importance. In addition to transporting photo-generated holes and preventing direct contact between the absorber layer and electrode, it also prevents moisture content in the perovskite absorber from degradation. Here, to further enhance the performance of our reference cell, CdZnS is used as an ETL and employed with six HTLs (NiO_x, Cu_2O, CuScN, PEDOT:PSS, PTAA, and CuI) of constant thicknesses. Their parameters are given in Table S5. The effect of these HTLs on device performance has been studied. Fig. 4(a) demonstrates the J-V characteristics, and EQE data is plotted in Fig. 4(b), whereas J-V parameters are presented in Table 6. The energy band diagram of different HTLs concerning the absorber and CdZnS is demonstrated in Fig. S3. Table 6 indicates that the best performance is achieved by CuI, followed by NiO_x and CuScN. The energy level band diagram in Fig. S3 indicates that these three layers have appropriate band alignment with the absorber layer, improving overall device performance. However, the performance of CuI relative to other HTLs is better in terms of higher J_{SC} and FF values due to its wider bandgap and better band alignment with the absorber layer. The performance of CuI can better be understood from the EQE data. It can be concluded from the EQE data that the optical absorption of CuI is better relative to other HTLs.

Similarly, the low performance of Cu2O is also varified from EQE data as it demonstrates low EQE. Our results could be better explained by considering the valence band offset (VBO) relative to HTL/perovskite interface with bandgap alignment. The VBO at the HTL/perovskite interface and built-in electric field (V_{bi}) is influenced by variation in the position of the valence band of the HTLs. The VBO can be described as $\chi_{HTL} + Eg_{(HTL)} - (\chi_{Perovskite} + Eg_{(Perovskite)})$ (Cheng et al., 2019). The values of VBO for different HTLs are tabulated in Table S6. Cheng et al. (Cheng et al., 2019) have reported that negative VBO value causes reduced V_{bi}, resulting in low Voc. In addition, a slight variation in VBO from negative to positive value lowers the charge interface recombination and results in higher FF in PSC (Minemoto and Murata, 2015). In our study, CuI displays a positive VBO of 0.01 eV as depicted in Table S6, which causes improved FF and overall PCE. In addition, high hole mobility and good transport characteristics of CuI are also essential parameters in obtaining improved device performance (Saranin et al., 2019).

Owing to high conductivity and high hole mobility of inorganic HTLs (CuI) (Pitchaiya et al., 2020; Yu and Sun, 2018), small thicknesses (~40 nm) demonstrated the best results in inverted PSCs (Wang et al., 2017). Sepalage et al. (Sepalage et al., 2015) reported no systematic variation in device performance due to CuI film thickness (ranging from 75 to 1000 nm). In addition, the CuI layer with 50 nm thickness was found experimentally to be highly transparent (>70%) from 450 to 800 nm range (Faustino et al., 2018). The high transparency permits a great number of photons flux to reach the perovskite absorber, resulting in an increased photocurrent generation. Therefore, we considered 50 nm thick CuI as HTL and performed further device optimization in the current work.

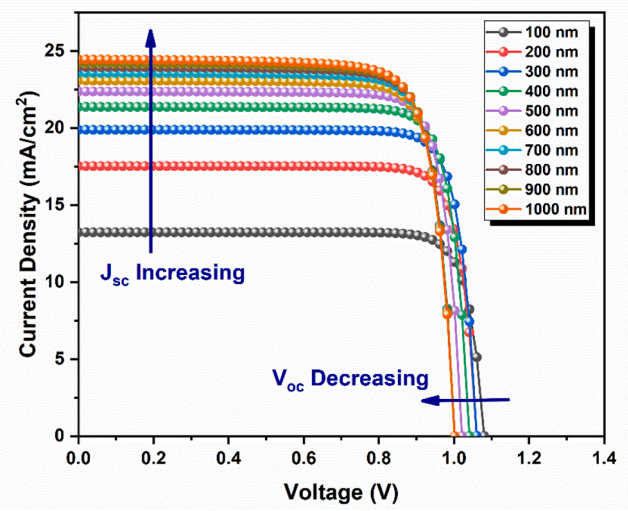

Fig. 5. The influence of absorber thickness variation on J-V characteristics of inverted PSC with CuI as HTL and CdZnS as ETL.

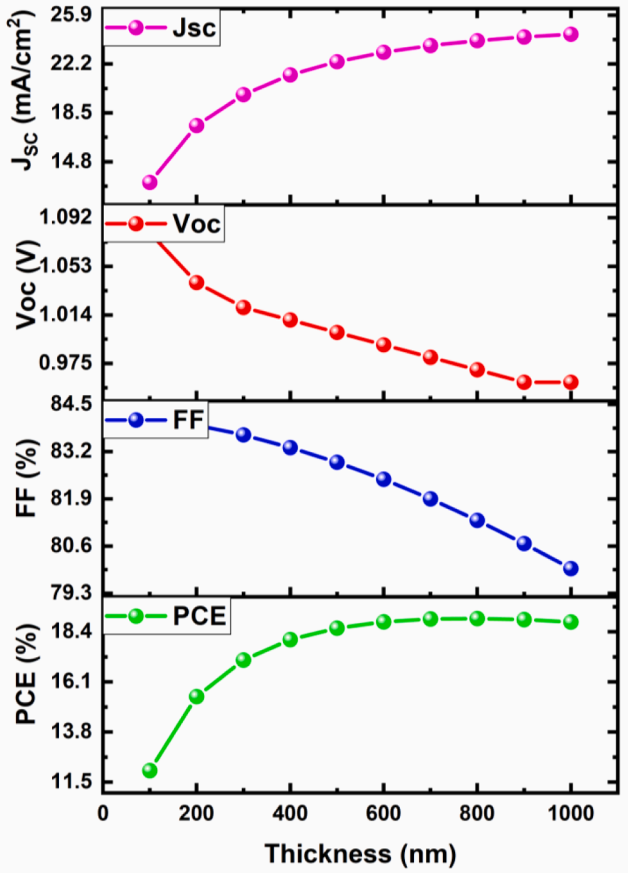

Fig. 6. The effect of absorber thickness variation on inverted PSC performance.

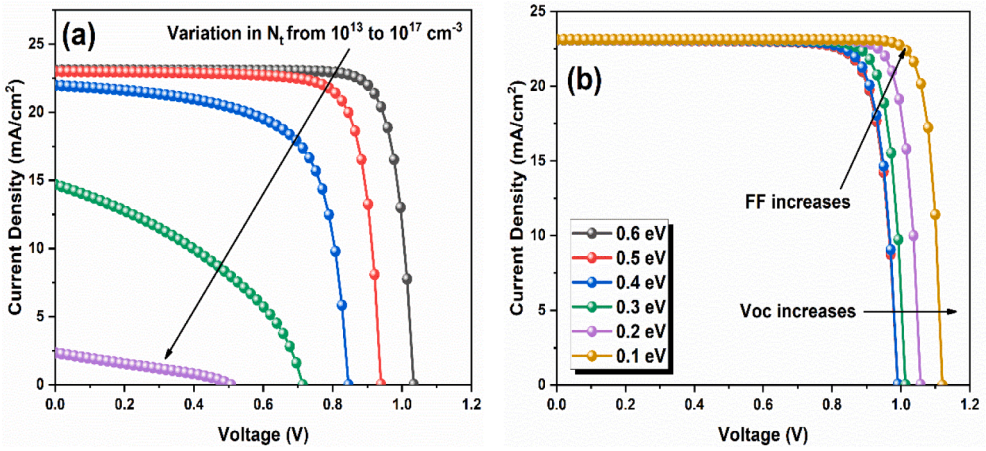

Fig. 7. Variation in J-V curves by varying (a) defect density (N_t) and (b) defect energy level of the perovskite.

3.4. Influence of variation in absorber thickness on PSC performance

The absorber thickness is another crucial parameter having a direct influence on device performance. Fig. 5 represents the resulted J-V curves with absorber thickness variation from 100 to 1000 nm, while the variation in J_{SC}, V_{OC}, FF, and PCE values is depicted in Fig. 6. From Fig. 6, it is indicated that an increase in the absorber thickness results in an increase in the J_{SC} and a decrease in V_{OC}. The increasing pattern of J_{SC} values is due to the increased amount of charge carrier generation. When the absorber layer thickness is small, the absorption rate for long-wavelength photons is lower, which produces a small amount of charge carrier generation and low J_{SC} results (Liu et al., 2014).

On the other hand, the small layer thickness causes low recombination, resulting in a high V_{OC}. With an increase in the absorber layer thickness, the absorption of long-wavelength photons also increases (Ghosh et al., 2020). This results in an increase in charge carrier generation and consequently an increase in J_{SC}. Albeit, with increased absorption, the recombination rate of carriers also increases since carriers have to cover a longer distance before reaching the respective electrodes. The increased rate of recombination results in low V_{OC}, as revealed in the simulation results of Fig. 5. The increase in absorber thickness increases the series resistance, which results in a drop in FF. The rise in PCE values is attributed due to an increase in J_{SC}. Our simulation results demonstrate that the optimal value for the absorber thickness should be 600 nm for the best performance inverted Cs-based triple cation PSC.

3.5. Influence of variation in defect density (N_t) and defect energy level of absorber

The other two essential processes that contribute to device performance are the charge carriers generation and recombination. When the material absorbs photons, electrons and holes (charge carriers) are produced. These charge carriers move to respective electrodes to form an electric current. However, the photo-generated charge carriers lost their lives due to perovskite absorber film low quality. This is attributed to the existence of a considerable number of defects that increase recombination and cause poor device performance. Therefore, the performance of PSCs is influenced by defect density as measured by recombination mechanisms and could be better explained by Shockley-Read-Hall (SRH) recombination, as defined by (4).

$$R^{SRH} = \frac{\upsilon_{TH} N_t \sigma_n \sigma_p [np - n_i^2]}{\sigma_p [p + p_1] + \sigma_n [n + n_1]} \quad (4)$$

Here, υ_{TH} represents the thermal velocity of the electron, N_t is the number of defects per unit volume, σ_n and σ_p are capture cross-sections of electrons and holes, n and p are the concentrations of the electron, the hole at equilibrium, n_i is the intrinsic number of density, p_1 and n_1 represent the concentrations of holes and electrons in valance band and trap defects, respectively.

Equation (4) indicates that defect density N_t is directly proportional to the R^{SRH}. In this study, the absorber defect density is varied from 1×10^{13} to 1×10^{17} cm^{-3}, and its influence on the performance of our simulated work is studied. J-V curves are plotted with variation in N_t values and shown in Fig. 7(a). Results demonstrate that by increasing the N_t from 1×10^{13} to 1×10^{17} cm^{-3}, a notable drop in J_{SC} from 23.11 mA/cm^2 to 2.35 mA/cm^2 and V_{OC} from 1.0334 V to 0.5462 V is observed. Since FF depends on V_{OC}, a remarkable drop in FF values (83.03% to 30.02%) can be noticed. These reductions in J_{SC}, V_{OC}, and FF values drastically decreased the PCE from 19.83% to 0.39%. This indicates that an increase in the N_t values causes a more significant number of defects, contributing to a higher recombination rate. Here, we set the N_t for the absorber as 2.6×10^{13} cm^{-3}, which accounts for carrier diffusion lengths of charge carriers (electron and hole) of 1.00 μm, according to the experimentally reported values (Stranks et al., 2013).

In addition, we examined the performance of our simulated work by varying the energy level of defects from 0.6 to 0.1 eV concerning below E_C considering $Nt = 2.6 \times 10^{13}$ cm^{-3}. Results are demonstrated in Fig. 7 (b). Variation in the defect energy level from 0.6 to 0.1 eV significantly affects V_{OC}, FF, and PCE values. However, it has a negligible behavior on J_{SC}. The V_{OC}, FF, and PCE values were boosted from 0.99 to 1.12 V, 82.44 to 87.85%, and 18.86 to 22.76%. In contrast, with a minor upsurge, the J_{SC} value changed from 23.09 to 23.12 mA/cm^2. Therefore, in this study, we set the defect energy level to be 0.1 eV.

3.6. Influence of variation in the absorber acceptor doping concentration (N_A)

The doping concentration has an essential effect on PSC performance. Depending on the type of dopants involved, doping may be classified as n-type and p-type. Therefore, selecting the proper value of acceptor doping concentration (N_A) is crucial for enhancing PSC performance. There are a variety of ways through which the doping concentration values can be varied experimentally. For instance, by introducing various dopants (Magnesium (Mg), sodium (Na), bismuth (Bi), tin (Sn) and titanium (Ti)) or varying their ratios with the absorber layer, doping concentration and defect density values can be varied experimentally (Bag et al., 2020). Also, by varying ratios of cesium (Cs), methylammonium iodide (MAI), formamidinium iodide (FAI), and lead iodide (PbI_2) is another technique that could be used to change doping concentrations and to minimize defects experimentally (Tian et al., 2020; Wang et al., 2014). Here, to comprehend the influence of doping on the PSC performance, the N_A of the absorber was changed from $1 \times$

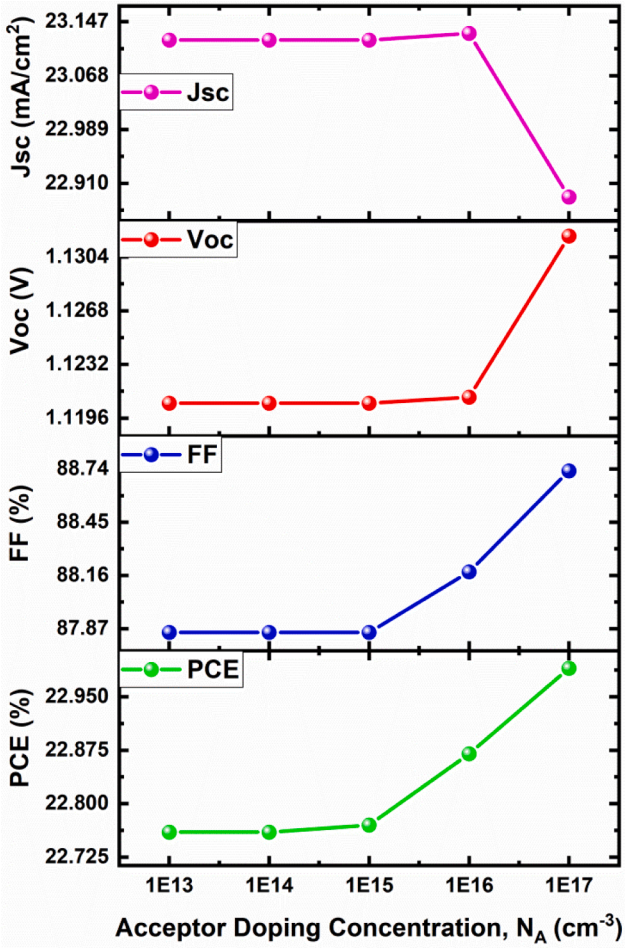

Fig. 8. Influence of absorber acceptor doping concentration variation on J-V parameters.

10^{13} to 1×10^{17} cm^{-3}, and the results are demonstrated in Fig. 8. Our results indicate that at low N_A levels, the J-V parameters have not changed. However, as the value of N_A exceeds 1×10^{15} cm^{-3}, the built-in electric field (V_{bi}) increases. An increase in V_{bi} results in better separation of photo-generated charge carriers and hence improves cell performance. At higher values of N_A, a decrease in Jsc was observed. A reduction in Jsc value with increasing N_A could be described by Auger recombination. At higher doping concentrations, Auger recombination increases, resulting in decreased device performance (Haider et al., 2018). Here, if we increase the N_A beyond 1×10^{17} cm^{-3}, a further decrease in Jsc was observed. Therefore, in the current study, we set 1×10^{17} cm^{-3} as the maximum value for N_A.

The relationship between V_{bi} and doping concentration can be best described by (5) (Ghosh et al., 2020).

$$V_{bi} = V_t \ln\left(\frac{N_A N_D}{n_i^2}\right) \tag{5}$$

Here, V_t is for thermal voltage, ni is for intrinsic carrier concentration, N_A, N_D are for charged impurities of acceptor and donor, respectively. Our results reveal a maximum PCE of 22.99% with an acceptor doping concentration of 1×10^{17} cm^{-3}.

3.7. Influence of variation in CuI and CdZnS doping concentrations

In addition to the absorber layer doping concentration, the HTL and ETL doping concentrations are also important parameters. In this work, doping concentrations of charge transport layers are varied from 1×10^{14} to 1×10^{22} cm^{-3}, and obtained results for HTL and ETL are presented in Fig. 9 and Fig. 10, respectively. The J-V parameters improve with the increase in the doping concentrations, as demonstrated in Figs. 9-10. For HTL doping concentration, low doping values cause barrier formation at the metal-semiconductor contact, blocking the flow of holes and resulting in recombination losses (Ahmed et al., 2020). On the other hand, an increase in the HTL doping values forms a strong V_{bi} at the HTL/perovskite interface, increasing the hole collection with enhanced hole conductivity by collecting more holes and repelling electrons from the HTL/perovskite interface. Our simulation results in Fig. 9 reveals that after a fixed point, the J_{SC}, V_{OC}, FF, and PCE values remain the same, and there is no further change in these values. Therefore, we considered 1×10^{20} cm^{-3} as the optimum value for the HTL doping concentration.

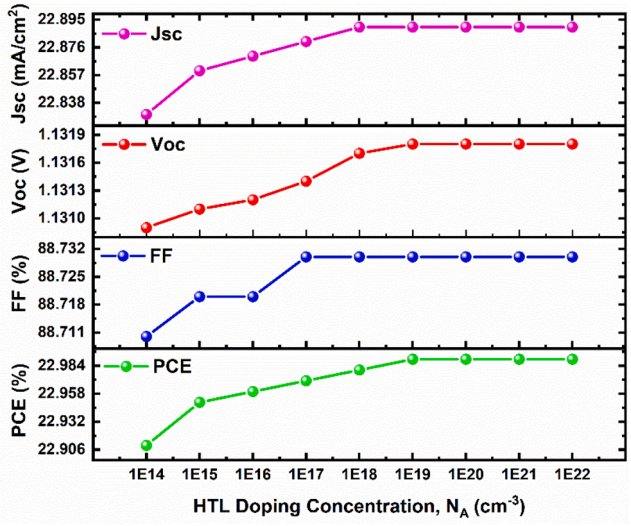

Fig. 9. Influence of CuI doping concentration variation on J-V parameters.

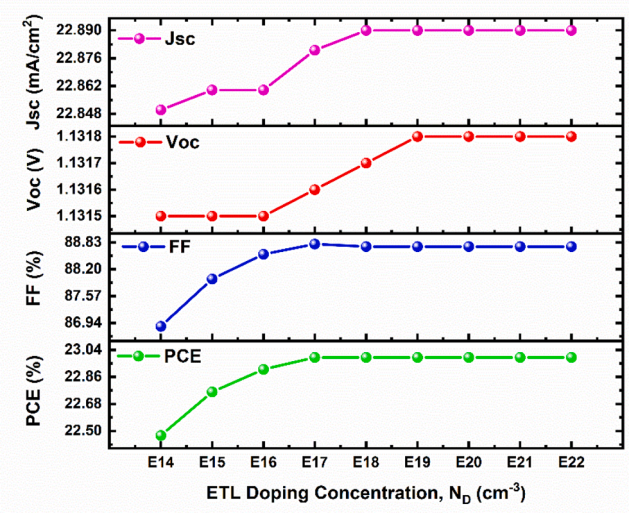

Fig. 10. Influence of CdZnS doping concentration variation on J-V parameters.

Similarly, the same process happens at the ETL side at high doping levels. High electron conductivity is developed due to forming a strong V_{bi} at the perovskite/ETL interface. This strong V_{bi} collects more electrons and repels minority charge carriers (holes), resulting in reduced interface recombination and improved device performance (Xu et al., 2018). Fig. 10 represents a constant behavior in J-V parameters at a specific point, and there is no further variation in J-V parameters. Hence, the optimum ETL doping concentration value is selected as 1×10^{20} cm^{-3}.

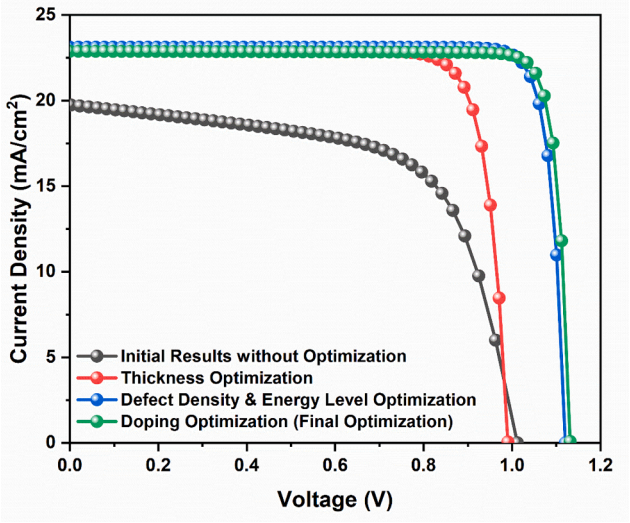

Fig. 11. A detailed comparison of different of J-V characteristics of inverted PSC starting from initial results to the final results via optimization of the absorber thickness (600 nm), optimization of defect density (2.60×10^{13} cm^{-3}) and energy level (0.1 eV), doping optimization of absorber (1×10^{17} cm^{-3}), HTL (CuI, 1×10^{20} cm^{-3}) and and ETL (CdZnS, 1×10^{20} cm^{-3}).

Table 7
A comparison of reported experimental work with our simulated work.

J_{SC} (mA/cm^2)	V_{OC} (V)	FF (%)	PCE (%)	Work Mode	Ref.
22.49	1.03	75.43	17.49		
23.05	1.05	76.08	18.41	Experiment	(Cao et al., 2019)
23.31	1.06	76.11	18.80		
22.89	1.13	88.73	22.99	Simulation	This work

Fig. 11 demonstrates the J-V curves of the various steps taken to optimize the inverted PSC. Here, the step-by-step optimization was performed through multiple processes such as absorber layer thickness, defect density, energy level optimization, and optimization of doping concentration. A detailed comparison of J-V parameters is also mentioned in Table S7. Finally, Table 7 compares already reported experimental work based on CuI as HTL with our proposed simulation study. By employing CuI in different working modes with triple cation perovskite and PCBM as ETL, J. Cao and fellows improved the efficiency values from 17.49 to 18.80% (Cao et al., 2019). However, we propose that by combining CuI and triple cation perovskite with wide bandgap CdZnS as a potential ETL, overall device parameters could be improved.

4. Conclusion

In a nutshell, the performance of inverted PSC based on ITO/HTL/(Cs/FA/MA)$PbI_{3-x}Br_x$)/ETL/Ag has been numerically examined through SCAPS-1D software. To improve the device performance, a comparative study was performed using a number of HTLs and ETLs. Our results demonstrated that CuI as HTL and CdZnS as ETL performed well compared to other HTLs and ETLs. To further boost the device performance, various measurement steps were taken like thickness variation of the absorber, optimization of defect density, defect energy level, doping optimization of the perovskite, CuI, and CdZnS. Results exhibited that variation in these parameters has an immense effect on device performance. A 600 nm thick value for triple cation perovskite absorber has been found as an optimum value. In addition, a strong built-in electric field, fast carrier mobility, increased conductivity caused by low defect density and defect energy level of the absorber, increased doping of the absorber, CuI, and CdZnS resulted in improvement in J_{SC}, V_{OC}, FF, and PCE of the inverted PSC. With such optimized values, our results produced the highest values of J_{SC} (22.89 mA/cm^2), V_{OC} (1.1318 V), FF (88.73%), and PCE (22.99%). Our findings proposed that CuI and CdZnS could be potential alternative replacements to existing costly, unstable, and high-temperature processed ETLs and HTLs. This study could pave the way to design and optimize planar inverted triple cation-based PSCs with improved performance.

Declaration of Competing Interest

The authors declare that they have no known competing financial interests or personal relationships that could have appeared to influence the work reported in this paper.

Acknowledgments

The authors are solely responsible for the conclusions reached in this paper. Furthermore, the authors are obliged to Prof. Marc Burgelman and his team at the University of Gent, Belgium, for granting access to SCAPS-1D simulation software.

Funding

This work was supported by the Qatar National Research Fund (QNRF, a member of the Qatar Foundation) under the NPRP award [grant number NPRP11S-1210–170080].

Data availability

Data will be available on reasonable request.

Appendix A. Supplementary material

Supplementary data to this article can be found online at https://doi.org/10.1016/j.solener.2021.08.008.

References

Ahmed, A., Riaz, K., Mehmood, H., Tauqeer, T., Ahmad, Z., 2020. Performance optimization of CH3NH3Pb (I1-xBrx) 3 based perovskite solar cells by comparing different ETL materials through conduction band offset engineering. Opt. Mater. 105, 109897. https://doi.org/10.1016/j.optmat.2020.109897.

Akbulatov, A.F., Ustinova, M.I., Shilov, G.V., Dremova, N.N., Zhidkov, I.S., Kurmaev, E. Z., Frolova, L.A., Shestakov, A.F., Aldoshin, S.M., Troshin, P.A., 2021. Temperature Dynamics of MAPbI3 and PbI2 Photolysis: Revealing the Interplay between Light and Heat, Two Enemies of Perovskite Photovoltaics. J. Phys. Chem. Lett. 12 (18), 4362–4367.

Alsalloum, A.Y., Turedi, B., Almasabi, K., Zheng, X., Naphade, R., Stranks, S.D., Mohammed, O.F., Bakr, O.M., 2021. 22.8%-Efficient single-crystal mixed-cation inverted perovskite solar cells with a near-optimal bandgap. Energy Environ. Sci. 14 (4), 2263–2268.

Ašmontas, S., Čerškus, A., Gradauskas, J., Grigucevičienė, A., Leinartas, K., Lučun, A., Petrauskas, K., Selskis, A., Sužiedėlis, A., Širmulis, E., Juškėnas, R., 2021. Cesium-Containing Triple Cation Perovskite Solar Cells. Coatings 11 (3), 279. https://doi.org/10.3390/coatings11030279.

Bag, A., Radhakrishnan, R., Nekovei, R., Jeyakumar, R., 2020. Effect of absorber layer, hole transport layer thicknesses, and its doping density on the performance of perovskite solar cells by device simulation. Sol. Energy 196, 177–182.

Bahtiar, A., Nurazizah, E.S., Latiffah, E., Risdiana, Furukawa, Y., 2018. Structural properties of perovskite films on zinc oxide nanoparticles-reduced graphene oxide (ZnO-NPs/rGO) prepared by electrophoretic deposition technique, AIP Conference Proceedings. AIP Publishing LLC, p. 030005.

Bai, S., Da, P., Li, C., Wang, Z., Yuan, Z., Fu, F., Kawecki, M., Liu, X., Sakai, N., Wang, J.-T.-W., 2019. Planar perovskite solar cells with long-term stability using ionic liquid additives. Nature 571 (7764), 245–250.

Burgelman, M., Nollet, P., Degrave, S., 2000. Modelling polycrystalline semiconductor solar cells. Thin Solid Films 361-362, 527–532.

Cao, J., Wu, B., Peng, J., Feng, X., Li, C., Tang, Y., 2019. Copper-copper iodide hybrid nanostructure as hole transport material for efficient and stable inverted perovskite solar cells. Sci. China Chem. 62 (3), 363–369.

Chen, H., Chen, Y., Zhang, T., Liu, X., Wang, X., Zhao, Y., 2021. Advances to High-Performance Black-Phase FAPbI3 Perovskite for Efficient and Stable Photovoltaics. Small Struct. 2 (5), 2000130. https://doi.org/10.1002/sstr.v2.510.1002/sstr.202000130.

Cheng, N., Li, W., Sun, S., Zhao, Z., Xiao, Z., Sun, Z., Zi, W., Fang, L., 2019. A simulation study of valence band offset engineering at the perovskite/Cu2ZnSn (Se1-xSx) 4 interface for enhanced performance. Mater. Sci. Semicond. Process. 90, 59–64.
Chowdhury, M.S., Shahahmadi, S.A., Chelvanathan, P., Tiong, S.K., Amin, N., Techato, K., Nuthammachot, N., Chowdhury, T., Suklueng, M., 2020. Effect of deep-level defect density of the absorber layer and n/i interface in perovskite solar cells by SCAPS-1D. Results Phys. 16, 102839. https://doi.org/10.1016/j.rinp.2019.102839.
Chowdhury, T.H., Ferdaous, M.T., Wadi, M.A.A., Chelvanathan, P., Amin, N., Islam, A., Kamaruddin, N., Zin, M.I.M., Ruslan, M.H., Sopian, K.B., 2018. Prospects of Ternary Cd 1–x Zn x S as an Electron Transport Layer and Associated Interface Defects in a Planar Lead Halide Perovskite Solar Cell via Numerical Simulation. J. Electron. Mater. 47 (5), 3051–3058.
Coulibaly, A.B., Oyedele, S.O., Aka, B., 2019. Comparative Study of Lead-Free Perovskite Solar Cells Using Different Hole Transporter Materials. Model. Numerical Simulat. Mater. Sci. 09 (04), 97–107.
Dixit, H., Punetha, D., Pandey, S.K., 2019. Improvement in performance of lead free inverted perovskite solar cell by optimization of solar parameters. Optik 179, 969–976.
Faustino, B.M.M., Gomes, D., Faria, J., Juntunen, T., Gaspar, G., Bianchi, C., Almeida, A., Marques, A., Tittonen, I., Ferreira, I., 2018. CuI p-type thin films for highly transparent thermoelectric pn modules. Sci. Rep. 8 (1), 1–10.
Firdaus, Y., Seitkhan, A., Eisner, F., Sit, W.Y., Kan, Z., Wehbe, N., Balawi, A.H., Yengel, E., Karuthedath, S., Laquai, F., 2018. Charge Photogeneration and Recombination in Mesostructured CuSCN-Nanowire/PC70BM Solar Cells. Solar RRL 2 (8), 1800095. https://doi.org/10.1002/solr.v2.810.1002/solr.201800095.
Ghosh, A., Dipta, S.S., Nikor, S.S.S., Saqib, N., Saha, A., 2020. Performance analysis of an efficient and stable perovskite solar cell and a comparative study of incorporating metal oxide transport layers. JOSA B 37 (7), 1966–1973.
Giovanni, D., Righetto, M., Zhang, Q., Lim, J.W.M., Ramesh, S., Sum, T.C., 2021. Origins of the long-range exciton diffusion in perovskite nanocrystal films: photon recycling vs exciton hopping. Light Sci. Appl. 10 (1), 1–9.
Haider, S.Z., Anwar, H., Wang, M., 2018. A comprehensive device modelling of perovskite solar cell with inorganic copper iodide as hole transport material. Semicond. Sci. Technol. 33 (3), 035001. https://doi.org/10.1088/1361-6641/aaa596.
Hima, A., Lakhdar, N., 2020. Enhancement of efficiency and stability of CH3NH3GeI3 solar cells with CuSbS2. Opt. Mater. 99, 109607. https://doi.org/10.1016/j.optmat.2019.109607.
Hoppe, H., Arnold, N., Sariciftci, N.S., Meissner, D., 2003. Modeling the optical absorption within conjugated polymer/fullerene-based bulk-heterojunction organic solar cells. Sol. Energy Mater. Sol. Cells 80 (1), 105–113.
Jeon, N.J., Noh, J.H., Kim, Y.C., Yang, W.S., Ryu, S., Seok, S.I., 2014. Solvent engineering for high-performance inorganic–organic hybrid perovskite solar cells. Nat. Mater. 13 (9), 897–903.
Jeong, J., Kim, M., Seo, J., Lu, H., Ahlawat, P., Mishra, A., Yang, Y., Hope, M.A., Eickemeyer, F.T., Kim, M., 2021. Pseudo-halide anion engineering for α-FAPbI 3 perovskite solar cells. Nature 592 (7854), 381–385.
Khattak, Y.H., Baig, F., Shuja, A., Beg, S., Soucase, B.M., 2020. Numerical analysis guidelines for the design of efficient novel nip structures for perovskite solar cell. Sol. Energy 207, 579–591.
Kojima, A., Teshima, K., Shirai, Y., Miyasaka, T., 2009. Organometal halide perovskites as visible-light sensitizers for photovoltaic cells. J. Am. Chem. Soc. 131 (17), 6050–6051.
Lakhdar, N., Hima, A., 2020. Electron transport material effect on performance of perovskite solar cells based on CH3NH3GeI3. Opt. Mater. 99, 109517. https://doi.org/10.1016/j.optmat.2019.109517.
Li, N., Zhu, Z., Li, J., Jen, A.K.Y., Wang, L., 2018. Inorganic CsPb1− xSnxIBr 2 for Efficient Wide-Bandgap Perovskite Solar Cells. Adv. Energy Mater. 8 (22), 1800525. https://doi.org/10.1002/aenm.v8.2210.1002/aenm.201800525.
Lin, L., Jiang, L., Li, P., Qiu, Y., Yan, Q., 2019. Numerical analysis of inverted-structure perovskite solar cell based on all-inorganic charge transport layers. J. Photonics Energy 9 (02), 1. https://doi.org/10.1117/1.JPE.9.024501.
Liu, D., Gangishetty, M.K., Kelly, T.L., 2014. Effect of CH3 NH3 PbI3 thickness on device efficiency in planar heterojunction perovskite solar cells. J. Mater. Chem. A 2 (46), 19873–19881.
Liu, T., Chen, K., Hu, Q., Zhu, R., Gong, Q., 2016. Inverted perovskite solar cells: progresses and perspectives. Adv. Energy Mater. 6 (17), 1600457. https://doi.org/10.1002/aenm.v6.1710.1002/aenm.201600457.
Liu, W., Wu, T., Liu, M., Niu, W., Chueh, Y., 2019a. Recent Challenges in Perovskite Solar Cells Toward Enhanced Stability, Less Toxicity, and Large-Area Mass Production. Adv. Mater. Interfaces 6 (9), 1801758. https://doi.org/10.1002/admi.v6.910.1002/admi.201801758.
Liu, X., Cheng, Y., Liu, C., Zhang, T., Zhang, N., Zhang, S., Chen, J., Xu, Q., Ouyang, J., Gong, H., 2019b. 20.7% highly reproducible inverted planar perovskite solar cells with enhanced fill factor and eliminated hysteresis. Energy Environ. Sci. 12 (5), 1622–1633.
Malerba, C., Biccari, F., Leonor Azanza Ricardo, C., D'Incau, M., Scardi, P., Mittiga, A., 2011. Absorption coefficient of bulk and thin film Cu2O. Sol. Energy Mater. Sol. Cells 95 (10), 2848–2854.
Meng, L., You, J., Guo, T.-F., Yang, Y., 2016. Recent advances in the inverted planar structure of perovskite solar cells. Acc. Chem. Res. 49 (1), 155–165.
Minemoto, T., Kawano, Y., Nishimura, T., Chantana, J., 2019. Numerical reproduction of a perovskite solar cell by device simulation considering band gap grading. Opt. Mater. 92, 60–66.
Minemoto, T., Murata, M., 2015. Theoretical analysis on effect of band offsets in perovskite solar cells. Sol. Energy Mater. Sol. Cells 133, 8–14.
Ou, Q., Bao, X., Zhang, Y., Shao, H., Xing, G., Li, X., Shao, L., Bao, Q., 2019. Band structure engineering in metal halide perovskite nanostructures for optoelectronic applications. Nano Mater. Sci. 1 (4), 268–287.
Petrović, M., Maksudov, T., Panagiotopoulos, A., Serpetzoglou, E., Konidakis, I., Stylianakis, M.M., Stratakis, E., Kymakis, E., 2019. Limitations of a polymer-based hole transporting layer for application in planar inverted perovskite solar cells. Nanoscale Adv. 1 (8), 3107–3118.
Pitchaiya, S., Natarajan, M., Santhanam, A., Asokan, V., Yuvapragasam, A., Madurai Ramakrishnan, V., Palanisamy, S.E., Sundaram, S., Velauthapillai, D., 2020. A review on the classification of organic/inorganic/carbonaceous hole transporting materials for perovskite solar cell application. Arabian J. Chem. 13 (1), 2526–2557.
Qiu, Z., Gong, H., Zheng, G., Yuan, S., Zhang, H., Zhu, X., Zhou, H., Cao, B., 2017. Enhanced physical properties of pulsed laser deposited NiO films via annealing and lithium doping for improving perovskite solar cell efficiency. J. Mater. Chem. C 5 (28), 7084–7094.
Raoui, Y., Ez-Zahraouy, H., Tahiri, N., El Bounagui, O., Ahmad, S., Kazim, S., 2019. Performance analysis of MAPbI3 based perovskite solar cells employing diverse charge selective contacts: Simulation study. Sol. Energy 193, 948–955.
Raoult, E., Bodeux, R., Jutteau, S., Rives, S., Yaiche, A., Coutancier, D., Rousset, J., Collin, S., 2019. Optical Characterizations and Modelling of Semitransparent Perovskite Solar Cells for Tandem Applications, 36th Eur. Photovolt. Sol. Energy Conf. Exhib. pp. 757-763.
Saranin, D., Gostischev, P., Tatarinov, D., Ermanova, I., Mazov, V., Muratov, D., Tameev, A., Kuznetsov, D., Didenko, S., Di Carlo, A., 2019. Copper Iodide Interlayer for Improved Charge Extraction and Stability of Inverted Perovskite Solar Cells. Materials 12 (9), 1406.
Sepalage, G.A., Meyer, S., Pascoe, A., Scully, A.D., Huang, F., Bach, U., Cheng, Y.-B., Spiccia, L., 2015. Copper (I) iodide as hole-conductor in planar perovskite solar cells: probing the origin of J-V hysteresis. Adv. Funct. Mater. 25 (35), 5650–5661.
Shamna, M.S., Nithya, K.S., Sudheer, K.S., 2020. Simulation and optimization of CH3NH3SnI3 based inverted perovskite solar cell with NiO as Hole transport material. Mater. Today: Proc. 33, 1246–1251.
Stranks, S.D., Eperon, G.E., Grancini, G., Menelaou, C., Alcocer, M.J., Leijtens, T., Herz, L.M., Petrozza, A., Snaith, H.J., 2013. Electron-hole diffusion lengths exceeding 1 micrometer in an organometal trihalide perovskite absorber. Science 342 (6156), 341–344.
Tian, J., Wang, J., Xue, Q., Niu, T., Yan, L., Zhu, Z., Li, N., Brabec, C.J., Yip, H., Cao, Y., 2020. Composition Engineering of All-Inorganic Perovskite Film for Efficient and Operationally Stable Solar Cells. Adv. Funct. Mater. 30 (28), 2001764. https://doi.org/10.1002/adfm.v30.2810.1002/adfm.202001764.
Wang, H., Yu, Z., Jiang, X., Li, J., Cai, B., Yang, X., Sun, L., 2017. Efficient and Stable Inverted Planar Perovskite Solar Cells Employing CuI as Hole-Transporting Layer Prepared by Solid-Gas Transformation. Energy Technol. 5 (10), 1836–1843.
Wang, Q., Shao, Y., Xie, H., Lyu, L., Liu, X., Gao, Y., Huang, J., 2014. Qualifying composition dependent p and n self-doping in CH3NH3PbI3. Appl. Phys. Lett. 105 (16), 163508. https://doi.org/10.1063/1.4899051.
Wang, S., Sun, W., Zhang, M., Yan, H., Hua, G., Li, Z., He, R., Zeng, W., Lan, Z., Wu, J., 2020. Strong electron acceptor additive based spiro-OMeTAD for high-performance and hysteresis-less planar perovskite solar cells. RSC Adv. 10 (64), 38736–38745.
Weber, S., Rath, T., Mangalam, J., Kunert, B., Coclite, A.M., Bauch, M., Dimopoulos, T., Trimmel, G., 2018. Investigation of NiO x-hole transport layers in triple cation perovskite solar cells. J. Mater. Sci.: Mater. Electron. 29 (3), 1847–1855.
Xu, L., Molaei Imenabadi, R., Vandenberghe, W.G., Hsu, J.W.P., 2018. Minimizing performance degradation induced by interfacial recombination in perovskite solar cells through tailoring of the transport layer electronic properties. APL Mater. 6 (3), 036104. https://doi.org/10.1063/1.5021138.
Ye, T., Petrović, M., Peng, S., Yoong, J.L.K., Vijila, C., Ramakrishna, S., 2017. Enhanced charge carrier transport and device performance through dual-cesium doping in mixed-cation perovskite solar cells with near unity free carrier ratios. ACS Appl. Mater. Interfaces 9 (3), 2358–2368.
Yu, Z., Sun, L., 2018. Inorganic Hole-Transporting Materials for Perovskite Solar Cells. Small Methods 2 (2), 1700280. https://doi.org/10.1002/smtd.v2.210.1002/smtd.201700280.
Zhao, P., Liu, Z., Lin, Z., Chen, D., Su, J., Zhang, C., Zhang, J., Chang, J., Hao, Y., 2018. Device simulation of inverted CH3NH3PbI3− xClx perovskite solar cells based on PCBM electron transport layer and NiO hole transport layer. Sol. Energy 169, 11–18.